FLOW MEASUREMENTS OF AN ISOLATED MODEL TILT ROTOR

Gloria K. Yamauchi
NASA Ames Research Center
Moffett Field, CA

Casey L. Burley
NASA Langley Research Center
Hampton, VA

Edzard Mercker and Kurt Pengel
Duits-Nederlandse Wind Tunnel
Noordoostpolder, The Netherlands

Ram JanakiRam
The Boeing Company
Mesa, AZ

Abstract

Wake measurements on the advancing side of a 0.25-scale V-22 isolated tilt rotor are presented and discussed. Three-dimensional wake geometry data were obtained using the Laser Light Sheet (LLS) technique. The position of wake segments relative to the rotor blade were acquired for a range of thrust and shaft angles. The rotation sense of the wake segments was determined. The lower thrust condition generated negative tip loading over a larger portion of the rotor disk than the higher thrust condition. At a higher thrust condition for the same shaft angle, the number of observed negative circulation vortices decreased. Two-dimensional velocity measurements were obtained using the Particle Image Velocimetry (PIV) technique. Three methods for averaging the PIV velocity data are discussed. Two of the methods account for vortex wander; both methods, however, require further refinement in order to determine which method provides more accurate results. The third method, which does not account for vortex wander, should only be used to obtain general features of the flow. For the vortices examined, approximately 100 PIV samples were determined to be sufficient for computing the average vortex core size and core circulation. The core size and core circulation of the negative vortices were smaller than the positive circulation vortices. The core tangential velocity appears to have a nearly linear relationship to the core size for the vortices examined. The fraction of total circulation in the core for both negative and positive vortices was found to be consistent with the Scully and Oseen vortex models.

Introduction

The NASA rotorcraft community has invested heavily in tilt rotor research in the last ten years to prepare for the impending arrival of this versatile vehicle in the commercial market. Investigations focussing on the prediction and reduction of tilt rotor noise generated during descent have gained increasing importance. During descent, the tilt rotor is in a helicopter configuration causing the rotor blades to interact with the rotor wake. This blade-vortex interaction (BVI) causes significant three-dimensional unsteady blade loads, which are manifested as high vibration and impulsive noise (Ref. 1).

Recent tilt rotor wind tunnel and flight tests have shown that BVI noise is the dominant noise source for a large range of operating conditions (Refs. 2-5). Understanding the evolution, convection, and dissipation of the rotor wake is critical in understanding and predicting BVI noise. Validation of aeroacoustic analyses requires wake measurements of increasing detail. These requirements include not only the three-dimensional wake geometry, but also the tip vortex core size and strength.

The Laser Light Sheet (LLS) technique has been successfully used to measure the rotor wake geometry of both model-scale (Ref. 6) and full-scale (Ref. 7) rotors. The application of this technique and the data reduction process of the resulting images have matured to the point of being relatively straightforward.

In the last decade, advances in digital camera resolution allowed planar measurement systems such as Particle Image Velocimetry (PIV) (Refs. 8-11) and Doppler Global Velocimetry (DGV) (Ref. 12) to acquire instantaneous velocity measurements over relatively large areas and volumes. PIV has been applied to a number of fluids experiments such as the turbulent wake of a cylinder (Ref. 13), the flow behind pitching airfoils (Ref. 14), flow over flapped and slatted airfoils (Refs. 15,16), free jets and turbulent boundary layers (Ref. 17), and wind turbine wakes (Refs. 18 and 19), to name a few. The PIV technique has only recently been applied to rotor flows (Refs. 20-25). PIV appears to be a technique that can provide the detailed measurements required by rotor aeroacoustic analyses. In particular, PIV measurements will be most useful in investigating the complex wake of a proprotor. Unlike conventional helicopter rotor blades, proprotor blades are highly twisted and can generate negative loading over a large area of the rotor disk. The negative loading causes multiple vortices to be shed thereby increasing the complexity of the required wake model.

Under the NASA Short Haul (Civil Tiltrotor) program (Ref. 26), an aeroacoustic tilt rotor model test was conducted in the Duits-Nederlandse Windtunnel - Large Lowspeed Facility (DNW-LLF) in 1998. The test was a joint effort of NASA, the U.S. Army and Boeing. The model tested was the isolated Tilt Rotor Aeroacoustic Model (TRAM), which is a 0.25-scale V-22 proprotor. The major test objectives were to obtain a benchmark database to validate the NASA tilt rotor noise prediction system Tiltrotor Aeroacoustic Code (TRAC), described in Ref. 3, and to expand the understanding of the flow physics and acoustic sources of tilt rotors. Acoustic directivity, blade surface pressures, performance, blade dynamics and wake geometry data were obtained for a range of advance ratios (including hover), shaft angles, and rotor thrust conditions. The TRAM was operated in helicopter and airplane mode configurations. The results from this test represent the first extensive database for an isolated proprotor (Ref. 27). Acoustic and blade airloads results from this test are provided in Refs. 5 and 28, respectively. This paper will primarily focus on the rotor wake measurements that include both the LLS and PIV data.

The rotor wake measurements were acquired for a range of tilt rotor operating conditions. The objective of the LLS measurements was to obtain the geometry of selected wake segments relative to the rotor blade on the advancing side. The objective of the PIV measurements was to obtain detailed velocity measurements of selected rotor wake vortices, in particular, those typically involved in BVI.

This paper provides a general description of the isolated TRAM, detailed descriptions of the LLS and PIV measurement set-up, and a discussion of the data processing procedures. Several methods for averaging the instantaneous PIV velocity data are presented and discussed. Wake geometry, vortex core size, and circulation distribution results are presented for a selected number of BVI conditions.

Model and Facility Description

The TRAM is a 0.25-scale V-22 isolated proprotor, which is nacelle-mounted on a motor housing/sting. Figure 1 shows the TRAM installed in the DNW-LLF 8- by 6-m open-jet test section. The 3-bladed proprotor has a diameter of 2.9 m. The model proprotor was operated at nominal tip speeds of 215 m/s and 201 m/s for operating conditions simulating helicopter and airplane mode, respectively. The proprotor, proprotor shaft and nacelle were fixed relative to each other with the rotor angle of attack changed by sting actuation. The proprotor was trimmed to zero 1/rev flapping. A detailed description of the TRAM and an overview of the TRAM experiment in the DNW-LLF are presented in Refs. 29 and 27, respectively.

Measurement Set-Up

The investigation area for both the LLS and PIV was on the advancing side of the rotor. Except for the camera, both measurement techniques were performed


Figure 1. Isolated TRAM installed in DNW-LLF (view from above and upstream of model; microphone array in foreground).

with the same set-up of laser and seeding system. Figures 2a and 2b show the experimental set-up for the LLS and PIV wake geometry measurements, respectively. The coordinates x' and z' on Fig. 2b are the local PIV image coordinates. The z' axis is parallel to the tunnel coordinate axis z and the x' axis is rotated (135 degrees as shown in Fig. 2b) with respect to the tunnel coordinate axis x.

The seeding used for the LLS and PIV was accomplished by a specially designed seeding rake located in the settling chamber immediately before the turbulence screen. The rake is 3m x 4m and is connected to two seed generators equipped with Laskin nozzles. Di-2-Ethylhexyl-Sebacat (DEHS) was used as the seed material. For the TRAM test an aerosol of 1 μm diameter particles were generated. Due to the contraction of the flow in the tunnel, the actual seeded area was approximately 1m in diameter at the rotor model location. The seeding rake was remotely moved both vertically and horizontally during testing to seed the area of interest.

Laser Light Sheet Measurement Description

The LLS measurements employed a large (wide), traversing light sheet to visualize several adjacent vortex cross sections in one frame along with at least one rotor blade. For this study, data were acquired when the blade was positioned at 45 degree azimuth. The light sheet, generated by one Nd-Yag-II laser, was traversed parallel to the freestream flow direction in increments of 0.200 m for a total range of 1.343m. Using this configuration, the light sheet typically intersected 2-4 vortex filaments at each measurement position. The light sheet was approximately perpendicular to the blade, as shown in Fig. 2a. Calibration of the image plane was accomplished by locating a calibration plate at one of the actual test measurement positions. The calibration plate contained a grid of known dimensions. The light sheet was adjusted to be parallel with the front side of the calibration plate. From the calibration image, the image magnification and exact location with respect to the rotor coordinate system were determined. Since the light sheet traversed parallel to the streamwise or x-axis of the rotor coordinate system, the different laser light sheet positions were easily determined with respect to the calibration location. A CCD (Charged Coupled Device) color video camera (JVC TK-1080E)
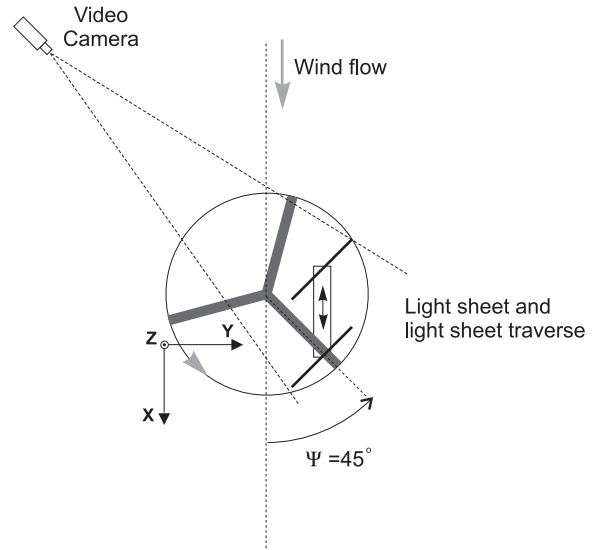
a) LLS set-up.
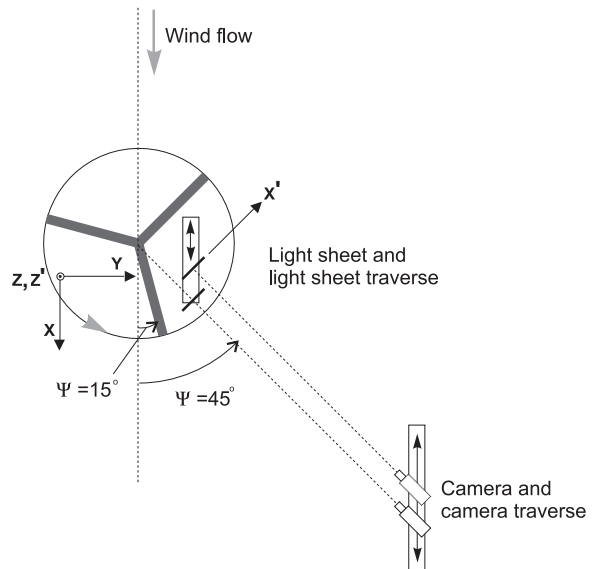
b) PIV set-up.

Figure 2. Schematics of the flow visualization set-ups within the test section.

was used in recording the LLS flow visualization images. The 0.5 inch CCD-chip has 681 (horizontal) by 582 (vertical) effective picture elements. The camera was operated in the usual video mode (interlaced), i.e. no external triggering and 1/50 sec shutter time. A video recorder then recorded the output signal from the camera. The recording rate is 25 full-frames per second or 50 half-frames. Due to the short flash duration (about 4 - 5ns) only one half-frame (of the full-frame) was exposed. Furthermore, due to the laser flash frequency limitation of 3.35 Hz, only every 15th half-frame on the videotape was exposed. The laser flash frequency was synchronized with the

rotor rotation frequency so that the half-frames captured on video correspond to the same blade azimuth position (i.e. 45 deg azimuth).

Particle Image Velocimetry Measurement Description

The PIV measurements were acquired in order to measure the vortex characteristics such as core size and strength. Thus, the PIV measurements were acquired at locations prior to a blade-vortex interaction where the vortices were not directly interacting with or influenced by the blade. The LLS recordings aided in the selection of these locations by providing a spatial 2-D view of the wake, which included several vortices as well as the blade. The PIV test setup is shown in Fig. 2b. All components of the PIV system were operated remotely from outside the test section.

Two Nd-Yag-II lasers were used to generate the light pulses. Each laser had a pulse energy of 280 mJ. The lasers were adjusted and optimized for a pulse frequency of 10 Hz. In order to obtain the maximum energy and a proper laser beam profile, the lasers must be operated in a narrow range around this frequency. Several lenses and mirrors were used to orient the light-sheet at the oblique angles indicated in Fig. 2b. The laser, first two mirrors and the traverse for the light sheet optics were rigidly mounted within the open jet test section underneath the rotor model. The light sheet was traversed parallel to the streamwise flow.

The PIV images were recorded using a full-frame, non-interlaced Kodak ES 1.0 Double-scan camera with external trigger. This camera was located on a tower that traversed parallel to the laser light sheet traverse. The line of sight of the camera was normal to the light sheet as shown in Fig. 2b. The 300 mm camera lens was adjusted by remote control. The Kodak ES 1.0 camera contains a chip with 1013x1008 usable pixels with a dynamic range of 8 bits and two AD converters, which double the speed for reading frames. In general, at least 100 image pairs were acquired at each condition, with the exception of two selected cases where 150 and 200 image pairs were obtained. The images were recorded at 3.35 Hz, which is the largest sample frequency attainable after synchronization of the camera, laser and rotor. A frame grabber in a PC, which was located on the lower part of the camera tower, collected the frames output by the camera. The PC

was operated remotely from outside the test section using a 50 m keyboard extension cable.

On-line evaluation of the PIV images was performed prior to data collection. The cross-correlation peak was determined over a small section of the image area. Several conditions were then imposed: the correlation peak is clearly recognizable; the number of spurious velocity vectors is less than 6; the minimum displacement is greater than 0.1 pixel; the maximum displacement is 8 pixels or less. Permanent data were collected if the above conditions were satisfied. For cases where these criteria were not met, adjusting the seeding as well as the delay time (either 20μs or 30μs) between particle images corrected the problem.

The PIV measurements were calibrated using a calibration plate. The plate, imprinted with a known grid, was positioned at the PIV measurement location. The light sheet was adjusted to be parallel with the front side of the plate. From the calibration image, the image magnification as well as the absolute location within the rotor coordinate system were determined. The position change caused by traversing the light sheet was calculated by adding the light sheet traverse position to the original x-location of the calibration plate. The light sheet traverse and the camera traverse were aligned parallel to the x-axis of the rotor coordinate system (Fig. 2b). Both traverses moved together insuring that the distance between the camera and light sheet remained constant.

The PIV recordings were obtained at specific rotor blade azimuth angles thus requiring rotor-laser-camera synchronization. A Hardsoft PCFS 2.0 phase shifter and sequencer controlled the timing of the camera with the laser using the rotor rpm as the input trigger. A spare-trigger adjusted the timing between the laser and the camera for variations in rotor rpm greater than 1% (approximately 14 rpm for this study), which was an acceptable tolerance for the laser. Additional details of the PIV system and acquisition are provided in Refs. 16 and 17.

Data Reduction Process

The LLS and PIV data processing methods are presented, including estimates of measurement uncertainty. Potential sources of error neglected in this study are also discussed.

LLS

Three-dimensional coordinates of the center of the vortex filament cross-sections were obtained from digitized images of LLS video recordings. The filament center was identified as the center of swirl or particle void for each vortex structure for each half-frame. Figure 3 shows a video half-frame capturing multiple vortices including a counter-rotating pair. Each vortex location presented in the Results section represents an average of 200 half-frame images taken in series (about 1 minute of recording time). As explained earlier, each image was recorded when the blade azimuth was 45 degrees. The wake geometry was recreated by performing this processing for each sheet location. The resolution of the LLS images is 2 mm per pixel. The estimated uncertainty in the location of the vortex centers presented in this paper is ± 2.28 mm.

PIV

Velocity vector fields were obtained from each PIV image-pair using the cross-correlation method (Ref. 9). All the image pairs were evaluated with a 64x64 pixel interrogation window size using 75% overlap. This results in a 60x60 2D velocity vector field covering an area of 20 cm by 20 cm. One to two vortices were typically captured within this image area.

PIV velocity vector fields usually contain a limited number of incorrectly determined vectors. These vectors can usually be identified by visually inspecting each field. Before the PIV velocity fields are utilized in further processing and analysis, these incorrect or spurious vectors should be identified and replaced. A method that automatically identifies and replaces these spurious vectors is presented in this section. Next, the definitions used to locate the vortex center and to compute the vortex core size and circulation are presented. Application of these definitions to processing the data are then presented. As will be discussed, care must be taken when determining average quantities from the PIV velocity
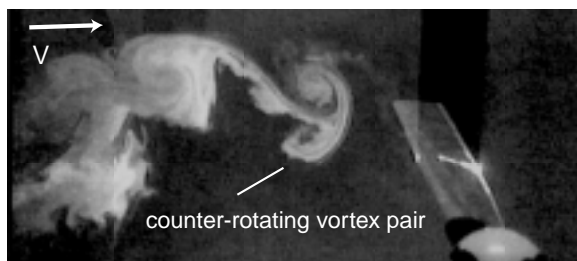

Figure 3. Sample LLS video half-frame.

fields. Thus, three methods for determining an average core size and circulation were investigated. This was done in order to evaluate the effects of vortex wander on the results and to provide an assessment of the variation in average results using different averaging procedures. The three averaging methods are presented and a discussion of the advantages and disadvantages is provided. The effect of the number of PIV samples on the averaged results is also included.

Removal of spurious vectors. PIV velocity vector fields can contain incorrect or spurious vectors (Ref. 9). Spurious vectors have a noticeably different magnitude and/or direction than the vector's nearest neighbors and are usually caused by a lack of sufficient particle-pairs in the interrogation region. Figure 4 shows an example of spurious vectors. Further processing of images containing spurious vectors will produce erroneous results. Westerweel (Ref. 30) was one of the first to provide a statistical analysis describing the occurrence of spurious vectors. As reported in Ref. 9 there are no general detection methods that can be applied universally to all flows; however, there are several algorithms that have been developed and tested for flows similar to the flow of this study. A procedure based in principle on mean value algorithms (Ref. 9) was developed for this study.

Mean value algorithms identify spurious vectors by comparing each individual velocity vector magnitude to some average magnitude. The present method computes the average velocity magnitude for a given instantaneous vector field. The ratio of each individual vector magnitude to the average magnitude was computed and compared to a user specified threshold ratio. If the ratio was greater than the threshold ratio, the vector was tagged as spurious. The threshold ratio used for this study was 1.5 and was determined by trial and error and verified by visual inspection.

After a vector was identified as spurious, the vector was replaced by the average of its neighbors in four directions: ±J (or x') and ±K (or z') where (J,K) represents the vector location in the 2D array. Four non-spurious neighbors in each of the four directions were used for this study. This number of neighbor vectors to include in the average was determined by trial and error. A sample result of the spurious vector identification and replacement process applied to the image in Fig. 4 is shown in Fig. 5.
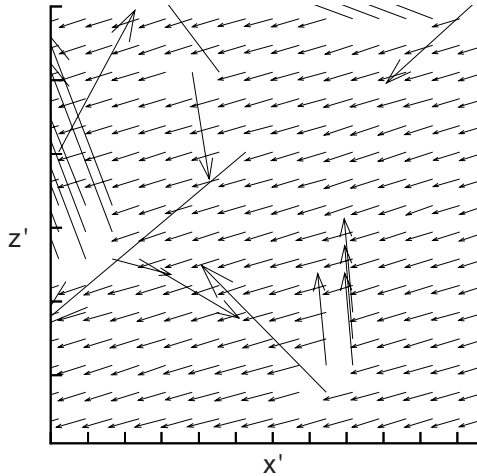
Figure 4. PIV image containing spurious vectors.
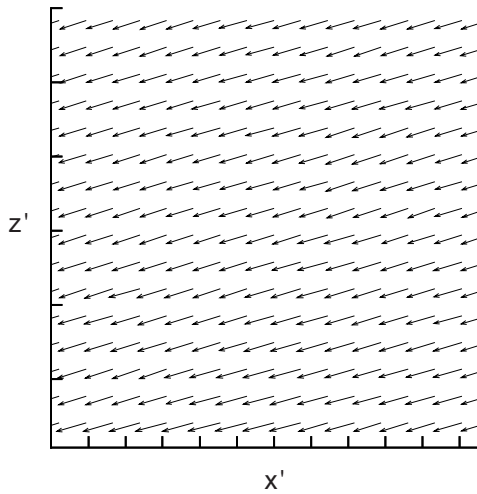

Figure 5. PIV image with spurious vectors of Fig. 4 replaced.

The replacement technique described above can lead to errors if the spurious vector is located in a region of high velocity gradient. In general, the spurious vectors observed in this study were near the edges of the field of view away from the area of interest containing a vortex.

Core size and core circulation estimation. The main objective of processing the PIV data was to determine vortex core size and core circulation. As mentioned earlier, three methods were used in this study to determine average vortex core size and circulation. All three of the methods require the location of the vortex center in order to determine the average or

instantaneous vortex velocity profile. A reasonable definition for the vortex center, as explained in Ref. 31, is the location of peak (maximum or minimum) vorticity. Thus, vorticity fields were computed from the appropriate (instantaneous or average) velocity fields using a center-difference scheme (Ref. 9). Since the velocity field is 2D, only one component of vorticity can be computed. Once the vortex center is known the velocity profile required (instantaneous or average) for each method is obtained.

Each averaging method uses either the instantaneous or average velocity profiles to determine the vortex core size and circulation. For this paper, the vortex core diameter is defined as the distance between the maximum and minimum peak velocity location of the velocity profile. The circulation in the vortex core is given by:

$$\Gamma_c = 2\pi r_c V_\theta \tag{1}$$

where V_θ is the tangential velocity at r_c and r_c is the core radius measured from the core center. V_θ is taken to be the half peak-to-peak velocity of a given velocity profile. These definitions are consistent with those commonly used in rotor wake prediction analyses (Ref. 32).

The three averaging methods used to compute an average vortex core size and circulation are: 1) identify the instantaneous vortex center and determine the instantaneous velocity profile passing through the center; align the profiles about the vortex center and compute an average profile; determine the core size and circulation from the average profile; 2) identify the instantaneous vortex center and determine the instantaneous velocity profile passing through the center; determine the core size and circulation from each instantaneous velocity profile; compute an average core size and circulation from the instantaneous results; 3) ensemble average the 100 instantaneous velocity fields; from the average velocity field identify the vortex center and determine the velocity profile passing through the vortex center; determine the core size and circulation from the velocity profile. Methods 1 and 2 eliminate the effect of vortex wander while Method 3 does not.

Method 1. Averaging using aligned velocity profiles. The initial step in this method was to locate the peak vorticity of each instantaneous velocity field. As a final filter for eliminating data influenced by spurious velocity vectors, a check for spurious peak vorticity

values (similar to that used for determining spurious velocity vectors) was implemented. An average peak vorticity of the 100 instantaneous peak vorticity values was computed. The ratio of each instantaneous peak vorticity to the average peak vorticity was computed and compared to a user input vorticity threshold ratio. In addition to this comparison, the sign of the instantaneous peak vorticity was compared to the sign of the average peak vorticity. Thus, an instantaneous vorticity peak was considered spurious if its ratio was greater than the input vorticity threshold ratio or if its sign was different than the average peak vorticity. The velocity field associated with this spurious vorticity was then discarded. Hence, the number of usable instantaneous velocity fields was reduced from the 100 available fields. The vorticity threshold values ranged from 1.25 to 1.5 for this study. The vorticity threshold ratio was determined by trial and error for each vortex analyzed.

If two vortices were present in the vorticity field, two searches for the peak vorticity were conducted with each search area limited to the area surrounding one vortex. Hence, a priori knowledge of the vortex's general location must be known so that the search area can be defined. The same search area was then used for all the instantaneous vorticity fields for a given test condition. Figure 6 shows instantaneous peak vorticity locations for one vortex at one test condition. The scatter of the peak vorticity locations
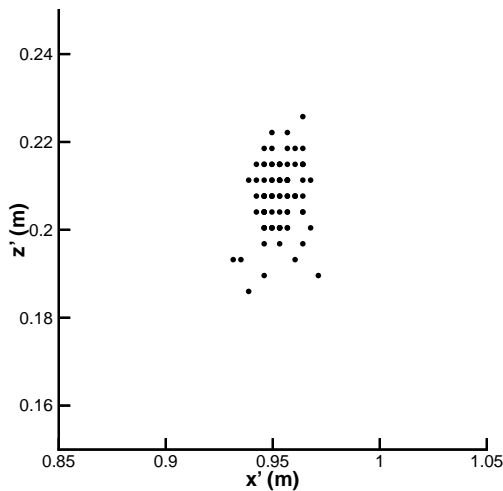
provides an indication and measure of the vortex wander.

After the instantaneous, non-spurious peak vorticity values were identified, the velocity profiles resulting from a horizontal (constant z') slice and a vertical (constant x') slice through the peak vorticity were aligned by co-locating the profiles about the individual vortex centers (i.e., peak vorticity location). For the present work, the directions of the slice were limited to the vertical and horizontal directions to simplify the process. After profile

a) subset of instantaneous samples
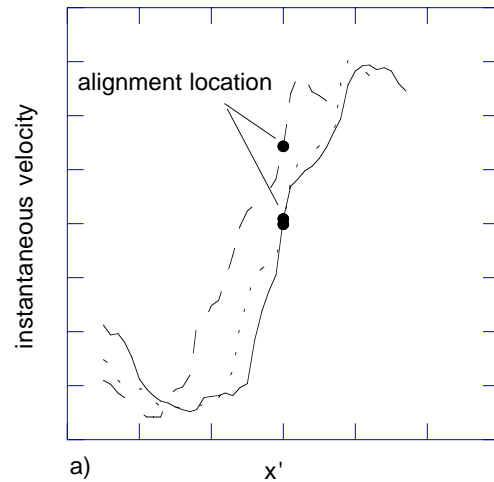
Figure 6. Peak vorticity locations identified from instantaneous vorticity fields.
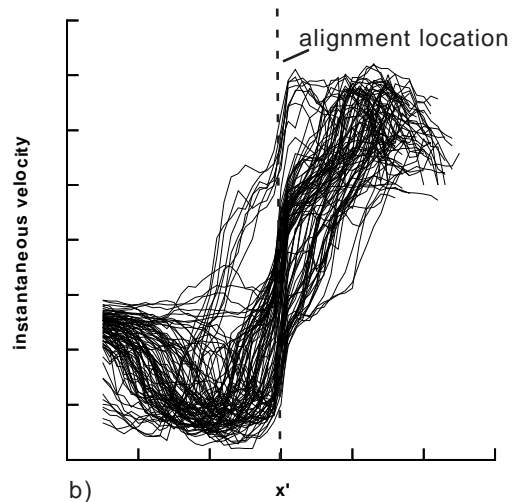
b) complete set of instantaneous samples

Figure 7. Instantaneous velocity profiles (horizontal slice) aligned about the location of peak vorticity (horizontal slice).

alignment, the instantaneous profiles were averaged. Figure 7 is a collection of instantaneous profiles from a horizontal slice through the corresponding peak vorticities. For clarity, Figure 7a shows only three of the profiles shown in Figure 7b. As shown in Figure 7a, the profiles are aligned using the x' location associated with each profile's peak vorticity location (determined from Figure 6). Figure 7a shows that the alignment technique is affected by the varying velocity gradient between the minimum and maximum velocity of each profile. This results in a larger than expected variation in velocity at each x' location as shown in Fig. 7b. The mid-point between the peak velocities of each profile is also a possible option for co-locating the profiles, if the laser sheet was perpendicular (i.e. orienting the image plane to minimize effects of the 3rd velocity component) to the vortex filament axis. Aligning at the velocity midpoint would then result in symmetric velocity profiles through the core. Figure 8 represents the average of the profiles in Fig. 7b with the velocity at the core subtracted. Depending on the amount of vortex wander, sections of an instantaneous profile may be undefined after alignment due to the limited size of PIV image. If a section of a profile was undefined, the velocity was set equal to zero and not included in the averaging. Using this alignment procedure, the number of samples available at each x' (or z') location varied. For each x' location of the velocity profile in Fig. 8, the number of samples used to determine each average value is indicated by the dashed line whose scale is given on the right vertical axis. Although 100 instantaneous vector fields were available, some fields were discarded because their peak vorticity values were identified as spurious. The vortex core size and circulation were then computed from the averaged profile.

Method 2. Averaging using instantaneous core and circulation values. This method used the same collection of instantaneous velocity profiles selected for the alignment process described in the previous section. The core diameter and core circulation were then computed for each instantaneous profile. The average and standard deviation of both core size and circulation were then computed. This method obviates the need for aligning the profiles while still accounting for vortex wander. However, as shown in Fig. 7, the instantaneous profiles are not smooth which makes the selection of the velocity minima and maxima sensitive to local disturbances in the profile including influences of the 3rd velocity component.
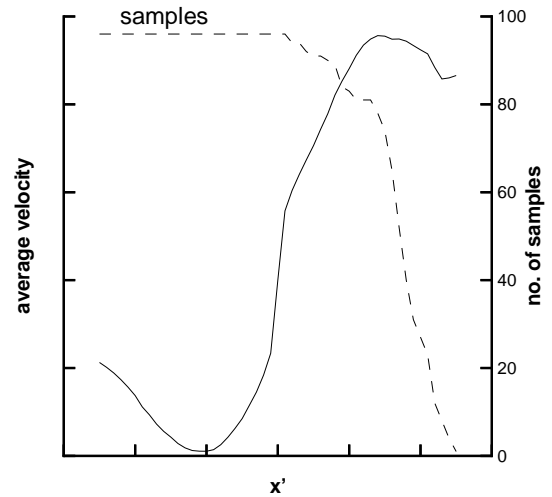

Figure 8. Averaged velocity profile after alignment.

Method 3. Ensemble averaging. For this method, the 100 instantaneous velocity fields are ensemble averaged. Ensemble averaging, which is the simplest to implement, can be used to obtain the general features (e.g. number of vortices, rotation sense) of the velocity or vorticity field. However, the method does not account for the effect of vortex wander, which will tend to produce a 'smeared' profile resulting in over estimation of the core size. Hence, this method should not be used for final estimates of core characteristics.
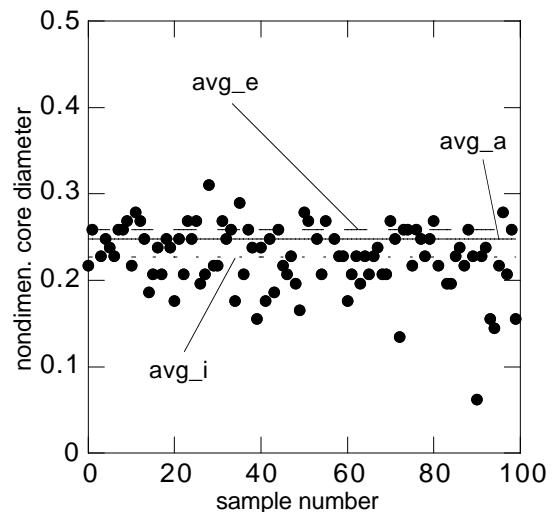

Figure 9. Instantaneous core size for the same vortex.

Figure 9 shows core size results computed using all three averaging methods. The results from Methods 1-3 are indicated by avg_a (aligned), avg_i (instantaneous) and avg_e (ensemble), respectively. The instantaneous core sizes used in Method 2 are also shown. Since Method 3 (ensemble) does not account for vortex wander, the computed core size is, as expected, larger than results from the Method 1 (aligned) or Method 2 (instantaneous). Although avg_e is larger than avg_a and avg_i, avg_e falls within the scatter of the instantaneous data. Because of the limitations (discussed earlier) of Methods 1 and 2, the ensemble averaged core size result did not always provide the largest value.

Sample population. An evaluation was performed to determine whether a sufficient number of PIV samples were available for computing average core sizes and circulations. The vortex analyzed in Fig. 9 was used for this evaluation. Out of 100 available samples for this vortex, 96 were identified as usable. The tangential velocity (V_θ) at the core radius which is related to the circulation by Eq.1, is used in this evaluation since V_θ is obtained directly from the PIV sample populations. The core diameter and V_θ were determined for each instantaneous velocity profile and are presented as filled circles in Figures 10 and 11, respectively. Moving averages and associated standard deviations (STD) were also determined for two sample sizes, N=25 (thin line) and N=50 (thick line) as well as the average using all the samples, N=96 (solid square symbols). Each moving average value is plotted at the center of the given sample set, i.e., n+N/2. For example, for N=25, the first average is determined from the first 25 samples, i.e. n_1=1 to n_{25}=25, and is plotted at n_1+N/2=13.5. The next average is determined using the next 25 samples, i.e. n_1=2 to n_{25}=26, and is plotted at n_2+N/2=14.5. This process is repeated until n_1=(n_{96}-N), for N=25 and 50 as shown in Figs. 10 and 11.

The average core diameter and average tangential velocity converged as N was increased from 25 to 96. Both the moving averages for core diameter and tangential velocity varied as much as 12% for N=25, and about 2% for N=50 from the average obtained using N=96. Thus, for computing average vortex core diameter and average tangential velocity, 50-96 samples was considered sufficient for this study. However, if details such as turbulence levels inside and outside the core are desired, much larger sample
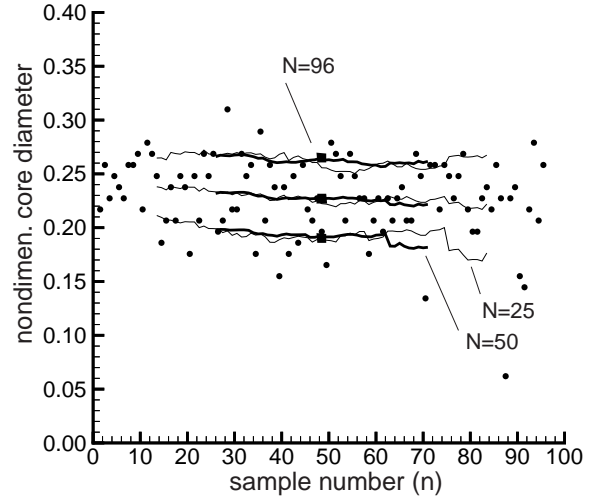

Figure 10. Average and STD of the core size using different sample sizes: N=25 (thin line); N=50 (thick line); N=96 (square symbol).
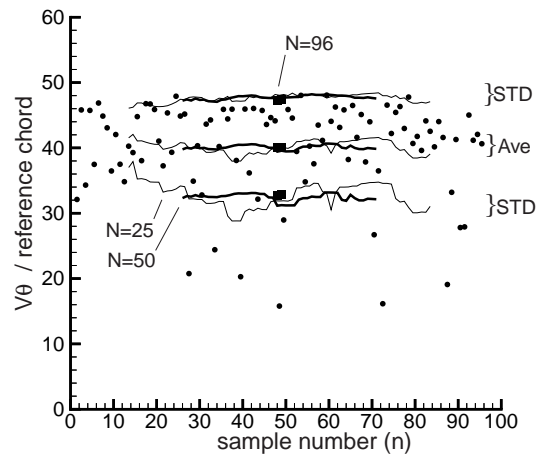

Figure 11. Average and STD of the tangential velocity at the core radius using different sample sizes: N=25 (thin line); N=50 (thick line); N=96 (square symbol).

sizes (typically on the order of five times) are required in order to establish confidence in the statistical quantities.

Results

The LLS measurements were acquired before the PIV data in order to assess the general features of the wake for various rotor conditions. A subset of the LLS test conditions was then selected for detailed scrutiny using the PIV technique. The PIV data reduction process described in the previous sections neglects

several key effects in calculating core size and circulation. The angle between the laser sheet and the vortex filament was unknown; therefore the core sizes presented in this paper are probably larger than the actual core size. The vortex convection velocity, defined here as the velocity at the vortex center, was subtracted from the velocity profile passing through the core. If the convection velocity varied over the core, the estimates for core size and circulation would be affected. Other considerations not explored in this paper include the presence of the 3rd velocity component, the influence of nearby vortices, effect of non-uniform seeding density, and distribution of PIV correlation levels across the PIV image. The results presented in this study should be evaluated with the above considerations in mind.

In this section, three-dimensional wake geometry measurements are provided for three shaft angles and two thrust conditions. Corresponding vortex size and circulation estimates are provided for one shaft angle and two thrust levels. All LLS and PIV data were acquired for an advance ratio of 0.15 and a nominal tip Mach number of 0.63.

LLS

Figures 12-14 show vortex filament locations with respect to the rotor blade for a low (negative), moderate (positive), and high (positive) shaft angle, respectively, for a low thrust condition. The shaft angle is defined as positive when the shaft is tilted aft. Each figure is comprised of a top view (a) and an edge view (from behind the blade) in a rotated coordinate system (b). The rotated coordinate system results from rotating the axes shown in Fig. 2a to account for the shaft angle and blade azimuth position, hence allowing an assessment of the blade-vortex separation distance. The blade azimuth was fixed at 45 degrees. The leading and trailing edge locations of the blade were also measured for each sheet location and are indicated in Figs. 12-14. The blade tip location, although not measured, is approximated and represented as a dotted line in the figures. The rotation sense of each filament is also identified, where counter-clockwise rotation (CCW) implies positive circulation and clockwise (CW) rotation implies negative circulation. The filament rotation sense is defined from the position of the PIV camera (Fig. 2b), not the LLS camera. Figures 12-14 show that there are roughly equal numbers of observed CCW and CW filaments. The presence of CW vortices suggests that the blade tip is negatively loaded and thus sheds a CW vortex at the tip and a

CCW vortex inboard of the tip. Figures 12-14 show that the angle between some of the CCW filaments and the blade are less parallel as compared with a simple single-vortex helical wake. If the CCW vortices were shed inboard of the tip, then the angle between the filament and blade would indeed be less parallel compared with a filament shed from the tip.

Although images such as Fig. 3 and plots such as Fig. 13 indicate that some of the CCW and CW vortices have combined into a pair, no data were acquired to determine the origin of each of these filaments. Therefore, the assumption cannot be made that a vortex pair originated from the same blade since the age of the vortices is unknown.

Figures 15-17 present results corresponding to the same shaft angles of Figs. 12-14, respectively, for a higher thrust condition. As the shaft angle is increased (more positive), the vortex-blade separation distance tends to increase (similar to Figs. 12-14). Comparing Fig. 15-17 to 12-14, there is an increased number of observed CCW filaments compared to CW filaments for the higher thrust condition for all three shaft angles, implying there is less negative loading on the blade. This observation is supported by the behavior of the differential leading-edge pressure near the blade tip shown in Figs. 18a and b for the low and high thrust conditions, respectively. For the low thrust condition (Fig. 18a) negative loading occurs over nearly the entire advancing side and about one-third (from 180 to 240 deg azimuth) of the retreating side. Figure 18b shows that the region and magnitude of negative loading is significantly reduced at higher thrust.

Figures 12-18 suggest that multiple vortices are being shed by one blade. Depending on the spanwise gradient of the bound circulation, combinations of positive and negative or multiple positive circulation vortices are possibly shed by a single blade. The streamwise spacing of the vortex filaments can typically be used to deduce the streamwise velocity magnitude and vice versa. Without knowledge of the filament origin, however, using the filament spacings in Figs. 12-17 to compute a streamwise velocity will result in erroneous values. The presence of multiple vortices greatly complicates the wake geometry and provides a very challenging system to model. Knowing the size and strengths of the CCW and CW vortices, however, is equally important as knowing the location of the vortices. The PIV measurements provide such information.
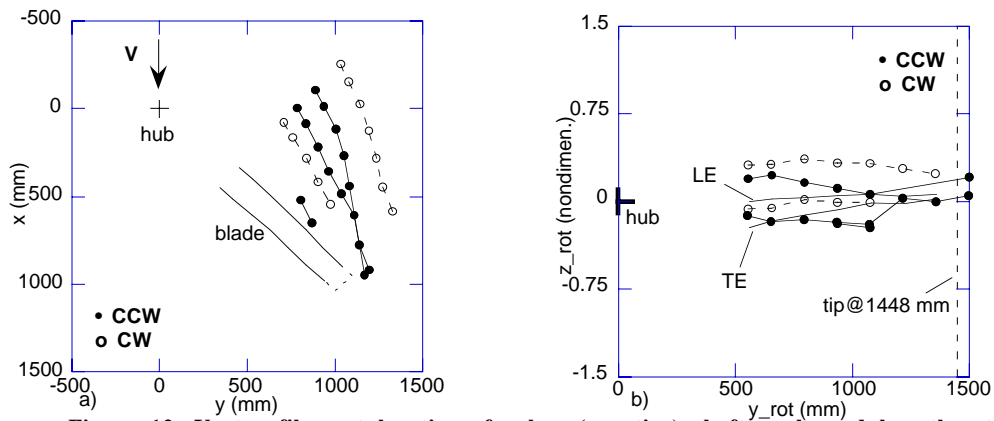
Figure 12. Vortex filament locations for low (negative) shaft angle and low thrust.
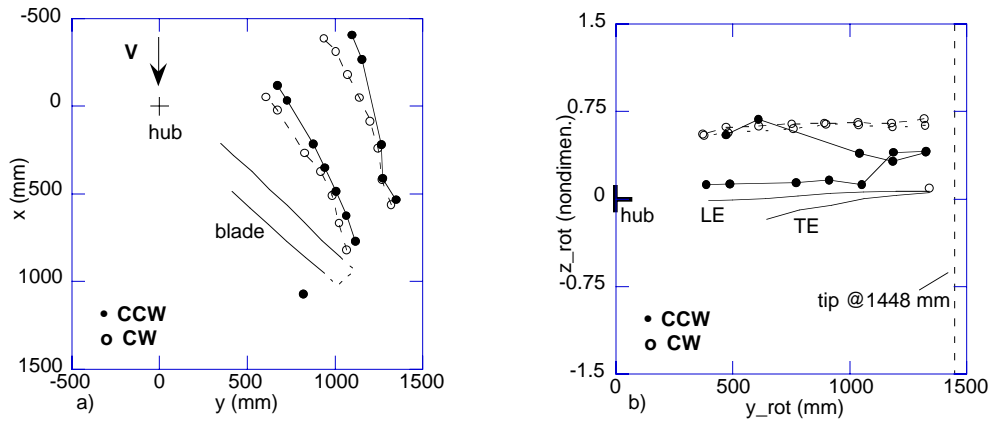**a) top view   b) view from behind blade, rotated coordinates**

Figure 13. Vortex filament locations for moderate (positive) shaft angle and low thrust.
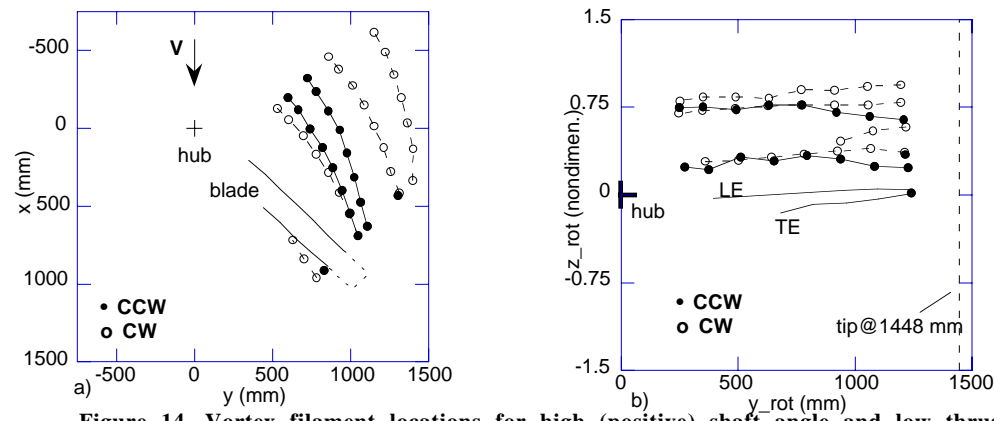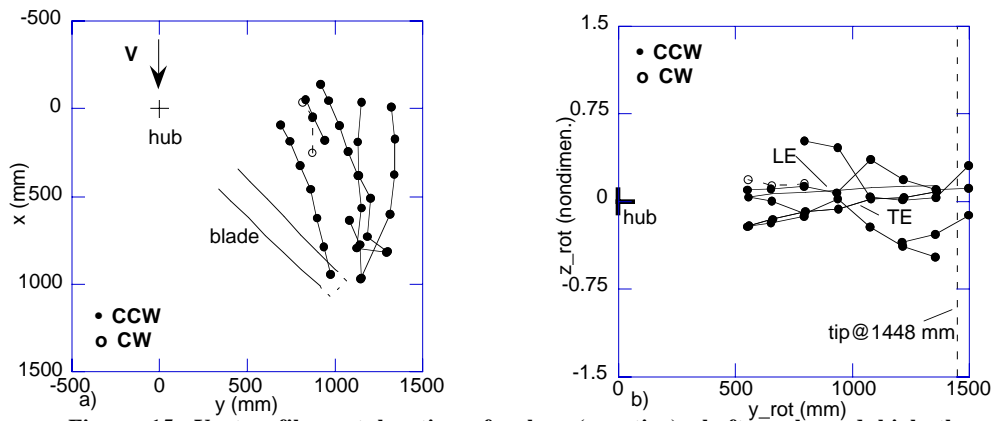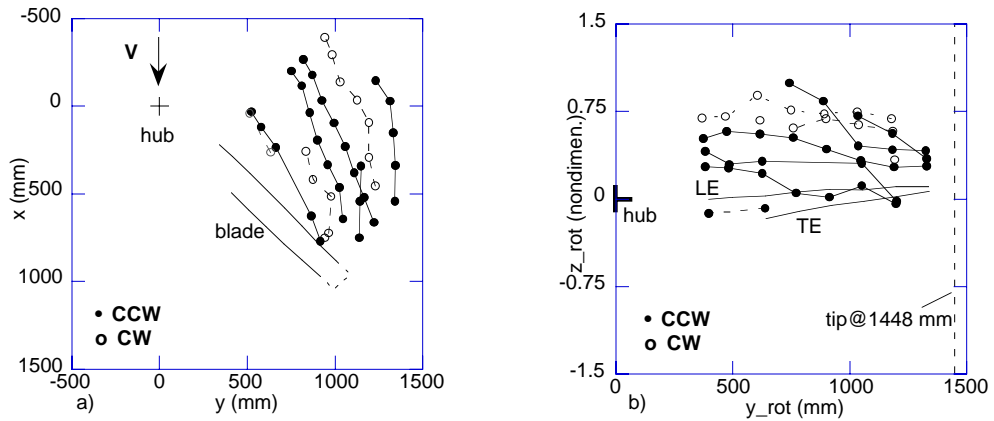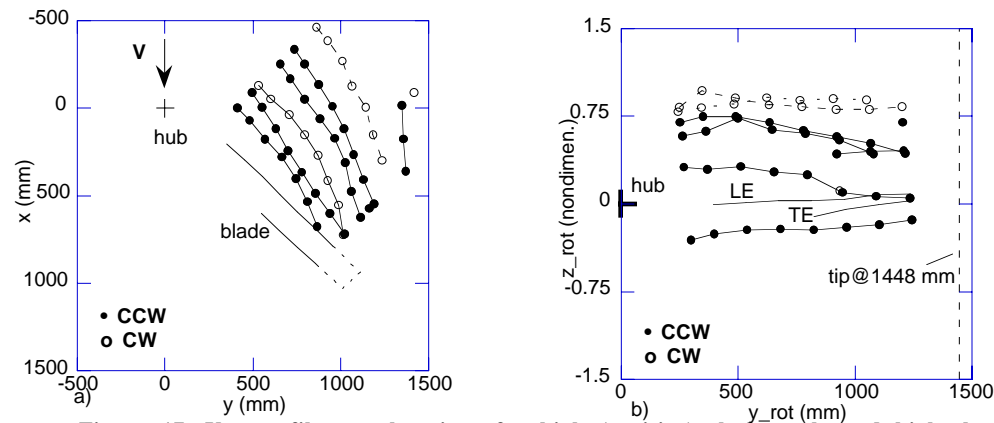**a) top view   b) view from behind blade, rotated coordinates**

Figure 14. Vortex filament locations for high (positive) shaft angle and low thrust.
a) top view   b) view from behind blade, rotated coordinates

Figure 15. Vortex filament locations for low (negative) shaft angle and high thrust.
a) top view   b) view from behind blade, rotated coordinates

Figure 16. Vortex filament locations for moderate (positive) shaft angle and high thrust.
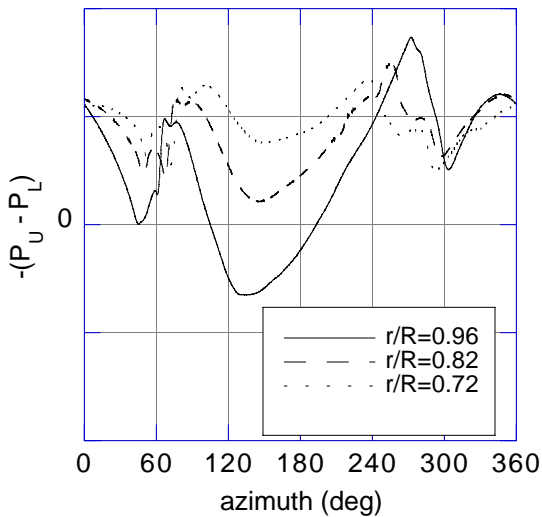**a) top view   b) view from behind blade, rotated coordinates**

Figure 17. Vortex filament locations for high (positive) shaft angle and high thrust.
a) top view   b) view from behind blade, rotated coordinates
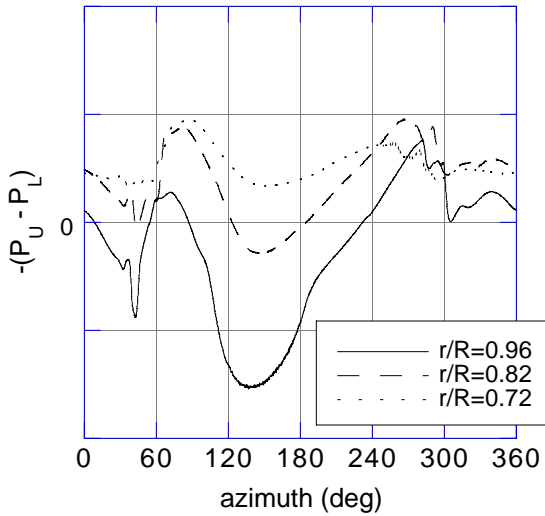
a) low thrust

b) high thrust

Figure 18. **Differential leading edge pressure near the blade tip.**

PIV

PIV images were acquired for a small number of test conditions. All measurements were acquired on the advancing side with the blade positioned at 15 deg azimuth with an advance ratio of 0.15 and tip Mach number of 0.63. The ages of the vortices are unknown since the vortices were not tracked from their origin. Hence, although two vortices sometimes appeared in the PIV field of view, one cannot assume that they originated from the same blade.

Figures 19a) and b) show instantaneous core size and core circulation results, respectively, for a CW vortex. The results were obtained from the horizontal cut through the vortex. This CW vortex was one of two vortices captured in a PIV field of view. The blade loading data for this test condition (moderate shaft angle, low thrust) is shown in Fig. 18a. The average core size and circulation values (obtained from the three averaging methods discussed in the previous section) are also presented.

In Fig. 19, avg_a refers to the value obtained by averaging the aligned velocity profiles (Method 1); avg_i corresponds to the average of the instantaneous values (Method 2); and avg_e refers to the values obtained by performing an ensemble average of the 100 vector fields (Method 3). Values for avg_a and avg_e fall within one standard deviation of avg_i. The distributions of both core size and circulation have the general shape of a normal distribution.

Figure 20 shows the core size and circulation results for the CCW vortex, which also appears in the same PIV field of view as the CW vortex of Figure 19. The CCW core sizes (Fig. 20a) from all three averaging methods are 2.0-2.5 times larger than that determined for the CW vortex (Fig. 19a). The CCW core circulations (Fig. 20b) are 2.5-3.0 times larger than the CW vortex (Fig. 19b). A plausible cause for this difference can be explained as follows. The CW vortex forms from the vorticity shed from the tip region. The CCW vortex forms from the vorticity shed inboard of the tip region. The spanwise extent of negative tip loading is likely to be smaller than the inboard spanwise extent of the positive blade loading. Hence, the inboard CCW vortex is expected to have a larger core size than the CW tip vortex.

Results for the same shaft angle but higher thrust condition are shown in Fig. 21. For this test condition, two CCW vortices were captured in the field of view. Only one CCW vortex was analyzed, however, since the second CCW vortex was too close to the field of view edge to be analyzed. The blade loading for this condition is shown in Fig. 18b. The tip is negatively loaded, but over a smaller spanwise extent and azimuth region compared to the low thrust test condition (Fig. 18a). The core size for the high thrust CCW vortex (Fig. 21a) is about 20%-30% smaller than the low thrust CCW vortex (Fig. 20a) and the corresponding core circulation is also 20%-45% smaller. This result is contrary to what is expected in hover. In hover, the higher thrust
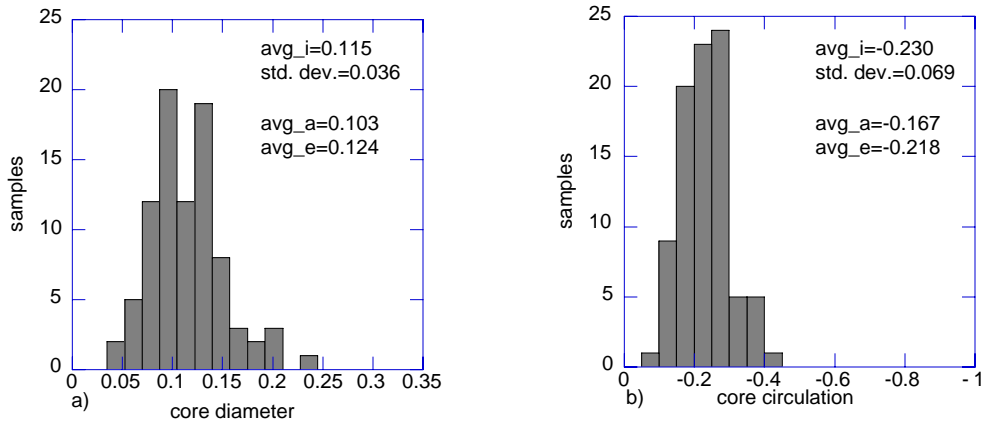
Figure 19. Distribution of instantaneous core quantities for a horizontal cut through a CW vortex at low thrust, moderate (positive) shaft angle.
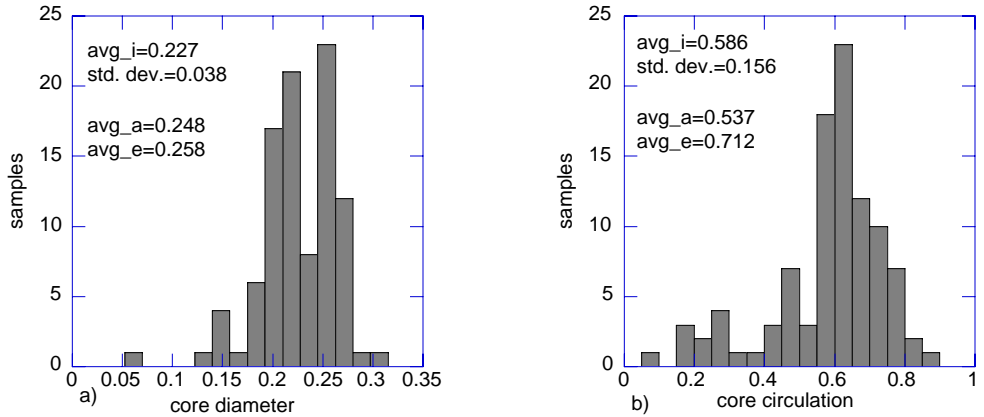**a) non-dimensional core diameter   b) non-dimensional core circulation**

Figure 20. Distribution of instantaneous core quantities for a horizontal cut through a CCW vortex at low thrust, moderate (positive) shaft angle.
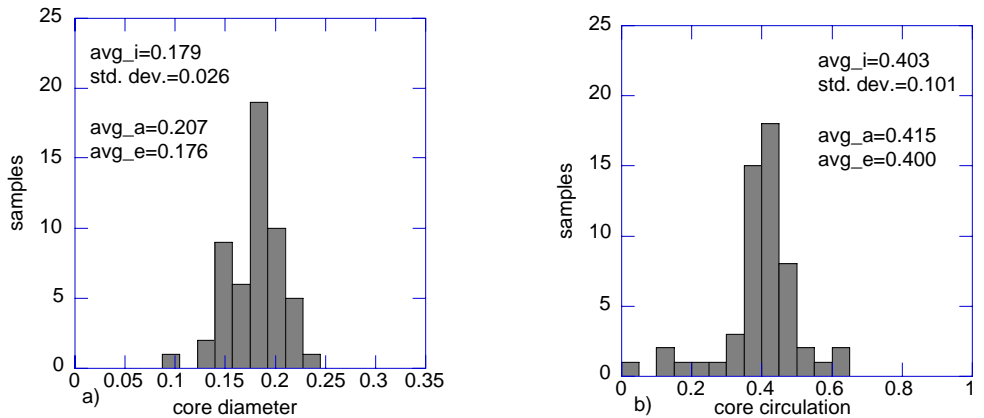**a) non-dimensional core diameter   b) non-dimensional core circulation**

Figure 21. Distribution of instantaneous core quantities for a horizontal cut through a CCW vortex at high thrust, moderate (positive) shaft angle.
a) non-dimensional core diameter   b) non-dimensional core circulation

condition is expected to generate a vortex with greater circulation than a lower thrust condition. In forward flight, however, the same reasoning cannot be applied since the blade loading varies greatly as a function of azimuth as shown in Fig. 18.

The above results appear to suggest that vortices with small core sizes also have lower circulation values, independent of the thrust (high or low) condition. To examine this relationship further, the tangential velocity of the core, (rather than the circulation) is plotted against the core size. In Figure 22 both the instantaneous and average values of core size and tangential velocity are shown for the 3 vortices examined in this study. The vortex tangential velocity appears to increase almost linearly with core size. This result, although based on limited data, is somewhat surprising since the vortices are of different rotation sense and from different thrust conditions. In addition, the data scatter is roughly circular in shape and similar for all three vortices, suggesting that the measurement and data processing variations associated with the vortex tangential velocity and core size are the same. Of course, additional data should be obtained to further define this relation. However, the results presented in Fig. 22 could be utilized in current wake models, which require vortex core size, and/or vortex tangential velocity as input parameters.

In addition to the core size and core strength, the fraction of the total circulation contained in the core is also informative for wake modeling purposes. Figures 23-25 present circulation as a function of distance from the core center for the vortices analyzed in Figs. 19-21, respectively. The circulation distributions were obtained from the average velocity profile computed using the aligned average (Method 1) and are presented for a horizontal cut (solid symbols) and vertical cut (open symbols) through the vortex center.

Two circulation distributions are determined from a given velocity profile, using Eqn. 1, by marching toward the minimum and maximum velocity location. The core radius, r_c, is defined as the distance from the core center to the x' location (for a horizontal cut) of the maximum (or minimum) velocity. A similar calculation is performed for a vertical cut resulting in four distributions per profile.
Figure 23 shows results for the CW vortex corresponding to Fig. 19. The velocity profile is not symmetric about the vortex center possibly due to the existence of a significant 3rd velocity component
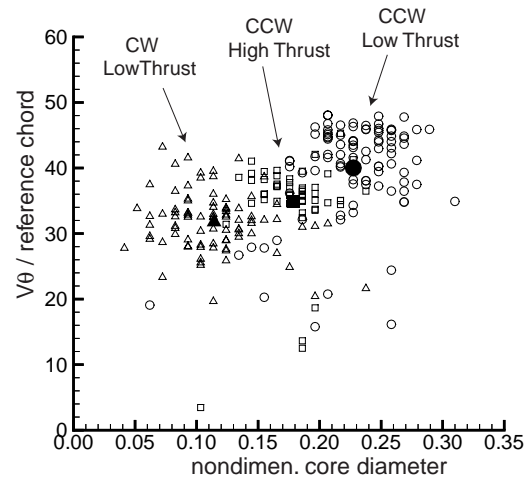

Figure 22. Vortex tangential velocity at the core radius versus core diameter. Solid symbols are the average values determined using averaging Method 2.

and/or because the field of view was not perpendicular to the vortex filament axis. The results from the horizontal and vertical cuts are similar, although the vertical cut results were determined from a smaller number of velocity vectors (approximately 25) than the horizontal cut (approximately 35-50). When two vortices were present in the field of view with one vortex above the other (as in the case of the vortices of Figs. 23 and 24), the field was divided roughly into an upper half and lower half. This reduced the number of vectors (for example, from 50 to 25) available for defining a velocity profile in the vertical direction, which contributed to more scatter in the results for the vertical cuts.

In Figure 23, the circulation in the CW vortex core is approximately 52% of the total circulation associated with this vortex. Figure 24, corresponding to the CCW vortex, shows that the core contains roughly 72% of the total circulation. The CCW vortex at the higher thrust condition, Figure 25, shows the core contains about 75% of the total circulation. These percentages are consistent with values assumed by vortex models often used in rotor wake calculations. The Scully vortex model (Ref. 32) assumes 50% of the total circulation is contained in the core while an Oseen vortex assumes 71%. Table 1 summarizes the results for the three vortices analyzed in this study.

Table 1. Nondimensional vortex core size and core circulation.

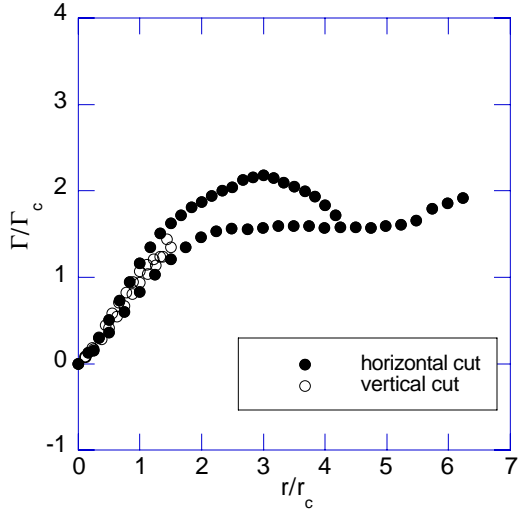| Thrust	Vortex rotation sense	core diameter: avg_i	core diameter: avg_a	core diameter: avg_e	core circ.: avg_i	core circ.: avg_a	core circ.: avg_e	% total circulation in core
low	CW	0.115	0.103	0.124	-0.230	-0.167	-0.218	~52%
low	CCW	0.227	0.248	0.258	0.586	0.537	0.713	~72%
high	CCW	0.179	0.207	0.176	0.403	0.415	0.400	~75%

Figure 23. Circulation distribution for a CW vortex: low thrust, moderate (positive) shaft angle
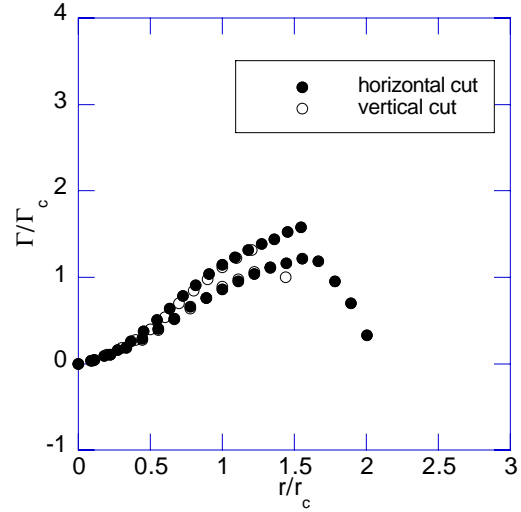

Figure 25. Circulation distribution for a CCW vortex: high thrust, moderate (positive) shaft angle
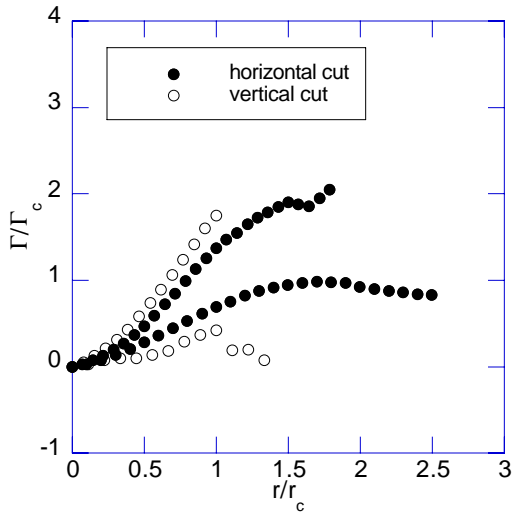

Figure 24. Circulation distribution for a CCW vortex: low thrust, moderate (positive) shaft angle

Concluding Remarks

Characterizing the complex wake system generated by blades shedding multiple vortices, as in the case of a proprotor, presents an immense technical challenge for both the experimentalist and analyst. This study provides quantitative information for a proprotor wake system. Using the LLS technique, the 3D wake geometry was measured on the rotor advancing side for two thrust conditions and several shaft angles. Two-dimensional velocity field measurements were acquired for selected vortices at two thrust conditions using the PIV technique.

Procedures for processing and averaging the PIV instantaneous velocity field data must be carefully considered and tested. This paper explored three methods for computing an average vortex core size and circulation from the PIV data. Two of the three methods accounted for vortex wander. Both methods,

however, require further refinement in order to determine which method provides more accurate results. The third method, which does not account for vortex wander, should only be used to obtain general features of the flow.

A sufficient number of PIV instantaneous velocities were required to obtain consistent results for average values of vortex core size and strength. For the evaluation performed, the average values based on 1/4 and 1/2 of the samples available (96) were found to differ up to approximately 12% and 2%, respectively, from the averages obtained using all available samples. Although 100 fields were acquired during the TRAM test, a significant number of fields were eliminated for some test conditions during PIV data validation due to spurious vorticity values. The number of instantaneous samples acquired during a PIV test should include a conservative estimate for the number of samples expected to be discarded during processing.

The following paragraph summarizes observations from this limited study.

The lower thrust condition generated negative tip loading that covered a larger portion of the rotor disk than the higher thrust condition. Both negative and positive circulation vortices were observed. Increasing the rotor thrust, while maintaining the same positive shaft angle, decreased the number of observed negative circulation vortices. The core size and core circulation of the negative vortices (which are a result of negative tip loading) were smaller than the positive circulation vortices. The tangential velocity at the core radius has a nearly linear relationship to the core size for the vortices examined. The fraction of total circulation in the core for both negative and positive vortices was found to be consistent with the Scully and Oseen vortex wake models. The results from this study although limited, are some of the first tilt rotor wake measurements available that offer quantitative values for average core size and circulation as well as wake geometry. These types of results are very much needed in advancing rotor wake prediction capabilities and should prove to be useful in guiding and setting parameter inputs for rotor wake analyses.

Acknowledgements

References

1. Schmitz F.H., "Aeroacoustics of Flight Vehicles: Theory and Practice; Vol. 1: Noise Sources," NASA RP-1258, Chapter 2, 1991.
2. Marcolini, M. A., Conner, D. A., Brieger, J.T., Becker, L.E., Smith, C.D., "Noise Characteristics of a Model Tiltrotor," AHS 51st Annual Forum, Fort Worth, TX, May 1995.
3. Burley, C.L., Marcolini, M.A., Brooks, T.F., Brand, A.G., Conner, D.A, "Tiltrotor Aeroacoustic Code (TRAC) Predictions and Comparison with Measurements," AHS 52nd Annual Forum, Washington, D.C., June 1996.
4. Conner, D. A., Marcolini, M. A., Edwards, B. D., Brieger, J. T., "XV-15 Tiltrotor Low Noise Terminal Area Operations," AHS 53rd Annual Forum, Virginia Beach, VA, April 1997.
5. Booth, E. R., Jr., McCluer, M., and Tadghighi, H., "Acoustic Characteristics of a Model Isolated Tiltrotor in the DNW," AHS 55th Annual Forum, Montreal, Canada, May 1999.
6. Mercker, E., Pengel, K., "Flow Visualization of Helicopter Blade Tip Vortices: A quantitative technique to determine the trajectory and the position of the tip vortex pattern of a model rotor," Eighteenth European Rotorcraft Forum, Avignon, France, September 1992.
7. Lau, B. L., Wadcock, A. J., Heineck, J. T., "Wake Visualization of a Full-Scale Tilt Rotor in Hover," AHS Technical Specialists' Meeting for Rotorcraft Aerodynamics and Acoustics, Williamsburg, VA, October 1997.

8. Adrian, R.J.: *"Particle Imaging Techniques for Experimental Fluid Mechanics,"* Annual Review of Fluid Mechanics, Vol. 23, p. 261-304, 1991.

9. Raffel, M., Willert, C., and Kompenhans, J., *Particle Image Velocimetry*, Springer-Verlag, 1998.

10. Lourenco, L.M., "Particle Image Velocimetry," von Karman Institute for Fluid Dynamics Lecture Series 1996-03.

11. Grant, I., "Particle Image Velocimetry: A Review," Proceedings Institute of Mechanical Engineers, 211, 1997.

12. Meyers, J.F., Fleming, G.A., Gorton, S.A, Berry, J., "Instantaneous Doppler Global Velocimetry Measurements of a Rotor Wake: Lessons Learned," presented at the 9th International Symposium on Applications of Laser Techniques to Fluid Mechanics, Lisbon, Portugal, July 1998.

13. Kompenhans, J., Reichmuth J., "2-D Flow Field Measurements in Wind Tunnels By Means of Particle Image Velocimetry," Proceedings of the 6th International Congress on Application of Lasers and Electro-Optics, San Diego, CA, 1987.

14. Crisler, W., Krothapalli, A., Lourenco, L., "PIV Investigation of High Speed Flow Over a Pitching Airfoil," AIAA 32nd Aerospace Sciences Meeting, Reno, January 1994.

15. Lourenco, L., Krothapalli, A., Smith, C.A., "Recent Advances in Particle Image Velocimetry," AGARD-Conference Proceedings 601, Symposium on Advanced Aerodynamic Measurements Technology, Seattle, WA, 1997.

16. Willert, C., Raffel, M., Kompenhans, J., "Recent Applications of Particle Image Velocimetry in Large-Scale Industrial Wind Tunnels," Proceedings of the 1997 17th IEEE International Congress on Instrumentation in Aerospace Simulation Facilities, ICIASF, Pacific Grove, CA, 1997.

17. Willert, C., Raffel, M., Kompenhans, J., Stasicki, B., Kaehler, C., "Recent Applications of Particle Image Velocimetry in Aerodynamic Research," Flow Measurement and Instrumentation, Vol. 7, (3-4), Sept-Dec 1996.

18. Whale, J., Anderson, C.G., "Application of Particle Image Velocimetry to Wind Turbine Wakes," Proceedings of SPIE, Vol. 2052, 1993.

19. Grant, I., Smith, G.H., Liu, A., Infield, D., Eich, T., "Particle Image Velocimetry Measurements of the Aerodynamics of a Wind Turbine," International Congress on Instrumentation in Aerospace Simulation Facilities, Silver Spring, MD, 1991.

20. Raffel M., Seelhorst, U., Willert, C., "Vortical Flow Structures At a Helicopter Rotor Model Measured by LDV and PIV*,"* Aeronautical Journal, Vol. 102, (1014), April 1998.

21. Raffel M., Willert C., Kompenhans J., Ehrenfried K., Lehmann G., Pengel K., "Feasibility and Capabilities of Particle Image Velocimetry (PIV) for Large Scale Model Rotor Testing," Heli Japan 98, Proceedings of the AHS International Meeting on Advanced Rotorcraft Technology and Disaster Relief, Gifu, Japan, April 1998.

22. Horner, M.B., Stewart, J.N., Galbraith, R.A.McD., Grant, I., Coton, F.N., "An Examination of Vortex Deformation During Blade-Vortex Interaction Utilising Particle Image Velocimetry," 19th Congress of the International Council of the Aeronautical Sciences, Vol. 2, 1994.

23. Saripalli, K.R., "Application of Particle Imaging Velocimetry Techniques to Helicopter Rotor Flowfields at McDonnell Douglas Aerospace," 33rd AIAA Aerospace Sciences Meeting and Exhibit, Reno, January 1995.

24. Murashige, A., Kobiki, N., Tsuchihashi, A., Nakamura, H., Inagaki, K., Yamakawa, E., "ATIC Aeroacoustic Model Rotor Test at DNW," AHS International Meeting on Advanced Rotorcraft Technology and Disaster Relief, Gifu, Japan, April 1998.

25. Murashige, A., Tsuchihashi, A., Tsujiuchi, T., Yamakawa, E., "Blade-Tip Vortex Measurement by PIV," Twenty-third European Rotorcraft Forum, Dresden, Germany, September 1997.

26. Marcolini, M. A., Burley, C. L., Conner, D. A., and Acree, C. W., Jr., "Overview of Noise Reduction Technology of the NASA Short Haul (Civil Tiltrotor) Program," SAE paper 962273, International Powered Lift Conference, Jupiter, FL, November 1996.

27. Young, L. A., Booth, Jr., E. R., Yamauchi, G. K., Botha, G. J., and Dawson, S., "Overview of the Testing of a Small-Scale Proprotor," AHS 55th Annual Forum, Montreal, Canada, May 1999.

28. Swanson, S., McCluer, M., Yamauchi, G., and Swanson, A., "Airloads Measurements from a 1/4-Scale V-22 Tiltrotor Wind Tunnel Test," to be presented at the 25th European Rotorcraft Forum, Rome, Italy, September 1999.

29. Young, L. A., "Tilt Rotor Aeroacoustic Model (TRAM): A New Rotorcraft Research Facility," AHS International Meeting on Advanced

Rotorcraft Technology and Disaster Relief, Gifu, Japan, April 1998.

30. Westerweel, J., "Efficient Detection of Spurious Vectors in Particle Image Velocimetry Data," *Experiments in Fluids*, Vol. 16, 1994.

31. Strawn, R.C., Kenwright, D.N., Ahmad, J., "Computer Visualization of Vortex Wake Systems," AHS 54th Annual Forum, Washington, DC, May 1998.

32. Johnson, W., *Helicopter Theory*, Princeton University Press, 1980.